Enhanced photoproduction of hydrogen on Pd/TiO$_2$ prepared by mechanochemistry

Yufen Chen [a,b], Lluís Soler [a,b,*], Marina Armengol-Profitós [a,b], Chenyang Xie [a,c], Daniel Crespo [a,c], Jordi Llorca [a,b,*]

[a] Institute of Energy Technologies and Barcelona Research Center in Multiscale Science and Engineering, Universitat Politècnica de Catalunya, Eduard Maristany 16, EEBE, Barcelona 08019, Spain
[b] Department of Chemical Engineering, Universitat Politècnica de Catalunya, Eduard Maristany 16, EEBE, Barcelona 08019, Spain
[c] Department of Physics. Universitat Politècnica de Catalunya, EEBE, Eduard Maristany 16, Barcelona 08019, Spain

ARTICLE INFO

ABSTRACT

Supported metal clusters are considered as promising cocatalysts in heterogeneous photocatalysis due to their singular geometric structures and unique reactivity. Nevertheless, to explore efficient synthetic routes that result in stable supported clusters with tailored active sites is an urgent yet challenging task. Here, a photocatalyst with highly dispersed Pd clusters onto TiO$_2$ is synthesized through only one-step ball milling procedure. The obtained Pd clusters form a particular metal-support interface, which has the ability to rearrange the small clusters evolving into Pd nanoparticles during the photocatalytic H$_2$ production process, and maintain a stable photocatalytic performance up to 100 h of continuous operation. Moreover, the unique interaction between Pd clusters and titania support was only observed in the ball-milled sample, and it disappeared after a calcination treatment. The mechanochemical strategy paves the way to stabilize supported metal clusters onto semiconductors without any organic compounds involved.

1. Introduction

Supported metal clusters and single atom catalysis have become one of the most promising new frontiers in heterogeneous catalysis. Supported metal clusters or atoms, which possess a high surface-to-bulk atomic ratio, can provide a new generation of highly-selective catalytic active sites for difficult reactions [1–3] and further minimize the noble metal loading. Different from metal nanoparticles, the distinct catalytic properties of metal clusters derive from the size-dependent geometric and electronic structures, high effective specific surface area and unique quantum confinement effect [4–6]. It has been demonstrated that the catalytic performance of supported metal clusters can be optimized by adjusting the number of atoms [7], size of the clusters [8–11], the specific atomic coordination [12] and the interaction between the support and metal species [13,14]. Although the supported metal clusters are typically more catalytically active than metal nanoparticles, it is well known that they tend to aggregate to form larger particles under thermal and/or light irradiation environments [15,16]. In general, the aggregation or sintering phenomenon that occurs in a

high-temperature reactive process can be explained by two typical mechanisms: particle diffusion/coalescence and Ostwald ripening [17–19]. In contrast, the aggregation that occurs under light irradiation has been not fully interpreted [4,20–23].

To enhance the photocatalytic stability under long-term operation, much effort has been devoted in the last decade to achieve the immobilization and stabilization of metal clusters on the surface of different supports. For instance, zeolite was used as a scaffold to encapsulate subnanometer silver clusters [24]; glutathione was employed to protect gold clusters [15,25] and 3-mercaptopropylsulfonate acted as a stabilizer for cobalt nanoclusters [26]. Despite recent advances in photocatalytic studies with stabilized metal clusters supported onto photocatalytic semiconductor materials, there continues to be a need for removing organic ligands or surfactants from the surface of nanoclusters when conventional stabilization strategies, such as thiol capping [27], microemulsions [28], vesicles [29], dendrimers [30], and water-soluble polymers [31], among others, are employed, in order to achieve their full activity and prevent side reactions and irreversible blocking of active sites. Despite the extensive research performed in the last decade,

---

optimizing the trade-off between stability and activity of supported clusters onto photocatalysts still remains challenging.

Herein, we aim to provide a facile, fast and solvent-free route to obtain an effective supported metal cluster photocatalyst by ball milling fabrication. Among the numerous available synthetic processes to produce heterogeneous catalysts, the mechanochemical strategy is simpler and cleaner than conventional wet chemistry-based syntheses. Recently, the mechanochemical strategy has gained the interest of researchers not only due to its "greener" performance but also to prepare advanced materials that cannot be obtained in solution [32–35]. In our previous research, we have successfully produced Au clusters highly dispersed on the surface of TiO$_2$ through a one-step ball milling procedure, but unfortunately the photocatalytic activity strongly decreased after three hours of reaction [36]. In the present article, we report the preparation of a novel Pd cluster/TiO$_2$ photocatalyst by a mechanochemical approach with a singular metal-support interaction between Pd clusters and TiO$_2$, which is a key factor to stabilize the photocatalytic activity in a hydrogen photoproduction process from water-ethanol under continuous operation. To the best of our knowledge, this special Pd cluster-TiO$_2$ interaction obtained by ball milling and suitable to perform photocatalytic reactions has not been described previously. We investigated the effect of the parameters influencing the fabrication of the photocatalysts: milling time, milling frequency and ball-to-powder ratio. We analysed the fresh and used Pd cluster/TiO$_2$ photocatalyst samples by means of several characterization techniques, including SEM, HRTEM, XRD, Raman, XPS, XANES, EXAFS and photoelectrochemical response among others, in order to understand the outstanding photocatalytic performance of the particular Pd cluster/TiO$_2$ architecture obtained.

2. Experimental section

2.1. Materials

Palladium (II) acetate (Acros Organics, 47.5% Pd), palladium nitrate hydrate (Acros Organics), palladium (II) chloride (Alfa Aesar), commercial TiO$_2$ P90 (Degussa) and commercial TiO$_2$ P25 (Evonik, purity > 99.55%) were used. Absolute ethanol and acetone were purchased from Scharlau. Milli-Q water (H$_2$O) was routinely used. All reagents were used without further purification.

2.2. Synthesis of Pd/TiO$_2$ ball milled photocatalysts

All the mechanochemical syntheses were carried out at a high-speed vibrating ball miller (Retsch, Mixer Mill MM200) as described elsewhere in detail [36]. In a typical ball milling (BM) procedure, palladium (II) acetate (0.0063 g) and commercial TiO$_2$ P90 (0.2937 g) were placed in a stainless-steel vessel (10 mL) together with one 15 mm diameter milling ball (13.54 g weight) to obtain a ball to powder ratio of 45 and Pd loading of 1 wt%. The mixture was milled for 10 min at the vibration frequency of 15 Hz. All the above-mentioned experimental conditions were routinely used unless otherwise noted. In order to study the effect of the milling parameters on the hydrogen photoproduction, a series of milling conditions were carried out, such as the vibration frequency (15–50 Hz), the ball to powder ratio (13–90) as well as the milling time (1–120 min). For each experiment, only one parameter was changed, and others were kept as constants. After milling, the obtained powder was denoted as Pd/TiO$_2$-BM. The ball-milled samples were employed for the photocatalytic tests without any further treatment.

2.3. Synthesis of reference photocatalyst samples

Palladium nitrate hydrate (0.0077 g) and palladium (II) chloride (0.0051 g) were used to obtain a nominal Pd loading of 1 wt% instead of palladium acetate for ball milling under the same conditions stated in Section 2.2, in order to explore the effect of metal precursors. The

resulting products were labelled as Pd(NO$_3$)$_2$/TiO$_2$-BM and PdCl$_2$/TiO$_2$-BM, respectively. Likewise, TiO$_2$ P90 was replaced by TiO$_2$ P25 in a typical BM process to study the effect of the TiO$_2$ support, denoted as Pd/P25-BM. As a comparison, the photocatalyst Pd/TiO$_2$ was synthesized by a conventional incipient wetness impregnation method (Pd/TiO$_2$-IWI), which has been described in detail elsewhere [37]. In brief, 0.0063 g of palladium acetate was dissolved in 5 mL acetone and the solution was then added dropwise to 0.2937 g of TiO$_2$ P90 powder. The obtained slurry was dried in an oven at 50 °C for 2 h and calcined in static air at 300 °C for 3 h. A mixture of Pd acetate and P90 was also prepared by grinding manually using an agate mortar and pestle for 10 min (labelled as Pd/TiO$_2$-MP). Finally, a Pd/TiO$_2$-BM sample was calcined at 300 °C for 3 h (labelled as Pd/TiO$_2$-BMC).

2.4. Catalyst characterization

The crystalline structure and phases of the photocatalysts were determined by X-ray diffraction (XRD) on a Bruker D8 diffractometer equipped with a Cu Kα radiation source (1.5418 Å), where the voltage and current were settled at 40 kV and 40 mA. The patterns were collected at room temperature in the 2θ-values ranging from 20° to 80° with a step of 0.02° and a dwell time of 1 s. The mean crystallite size of TiO$_2$ was determined according to the Scherrer formula based on the full width at half maximum (FWHM) at 2θ of 25.3°. Raman measurements were performed on a confocal Raman spectrometer (Renishaw in Via Qontor) employing a Leica DM2700M microscope (magnification 50 ×). The spectra were gathered with a 532 nm laser excitation and 2400 lines mm^{-1} of grating in the range of 50–800 cm^{-1} with 1 mW cm^{-2} laser energy. The actual loading amount of Pd was quantified by Inductively Coupled Plasma-Optical Emission Spectrometry (ICP-OES, Perkin Elmer Optima 3200RL). The morphology of the samples was studied by scanning electron microscopy (SEM) using a Zeiss Neon40 Crossbeam workstation at 5.0 kV equipped with a field emission source. Particle size statistics were conducted with the ImageJ software. High-resolution transmission electron microscopy (HRTEM) and scanning transmission electron microscopy under high-angle annular dark field mode (HAADF-STEM) were carried out on a FEI Tecnai F20 electron microscope equipped with a field emission electron gun with an accelerating voltage of 200 kV. At least one hundred Pd particles in each photocatalyst were considered for estimating the particle size distribution. Ultraviolet-visible diffuse reflectance spectra were acquired with a UV–VIS–NIR spectrometer (Shimazu UV-3600). The spectra were measured against BaSO$_4$ at a wavelength range of 200–800 nm. The obtained diffuse reflectance data were converted to absorbance spectra by means of the Kubelka-Munk function. Band gap energies (E$_g$) were evaluated by Tauc plots of $[F(R_\infty) E]^{1/2}$ versus photo energy E, where R_∞=R$_{Sample}$/R$_{BaSO4}$. The steady-state photoluminescence (PL) spectra were acquired with a fluorescence spectrometer (Cary Eclipse) under an excitation of 300 nm. X-ray photoelectron spectroscopy (XPS) was performed on a SPECS system equipped with a PHOIBOS 150 EP hemispherical energy analyser, a MCD-9 detector and an XR-50 X-ray source operating at 150 W. The C 1s signal at 284.8 eV was used as the reference to calibrate the binding energy (BE). X-ray absorption near edge structure (XANES) and extended X-ray absorption fine structure (EXAFS) at Ti K edge and Pd K edge were collected at ALBA Synchrotron Light Source, BL22-CLAESS beamline. Data pre-treatment and EXAFS reduction were performed using the DEMETER software package. For Ti K edge, the Fourier Transform (FT) was simulated on k^3-weighted EXAFS oscillations in the range of 3–12.8 Å and R space range of 1–3 Å.

2.5. Electrochemical and photoelectrochemical measurements

The photoelectrochemical (PEC) performance was evaluated on a Bio-logic Sp-200 (Bio-Logic Science Instruments, France) potentiostat/galvanostat in a three-electrode configuration containing an aqueous solution of 25 mL 0.5 M Na$_2$SO$_4$ as electrolyte (pH=7). A fluorine doped
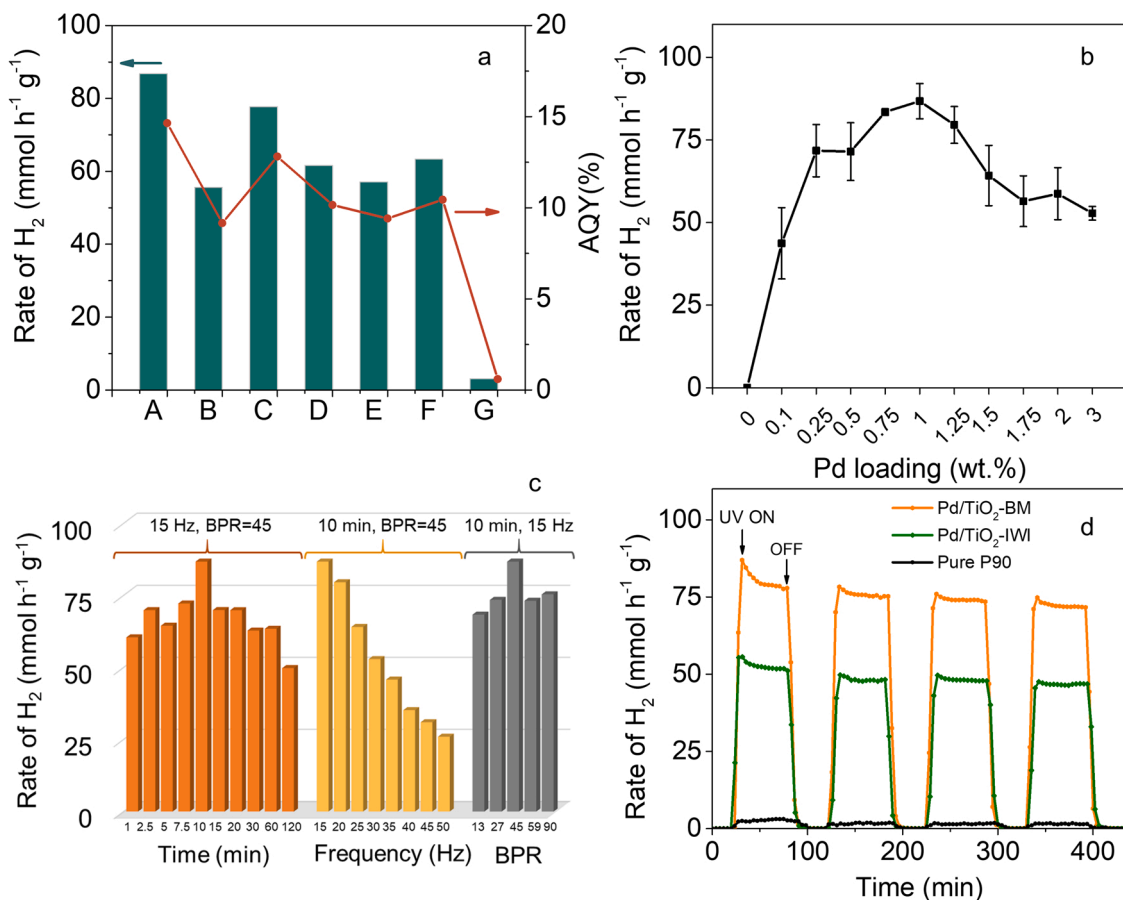
Fig. 1. (a) Comparison of the rate of hydrogen production and the corresponding AQY obtained over the following photocatalysts: (A) Pd/TiO$_2$-BM, (B) Pd/TiO$_2$-IWI, (C) Pd/TiO$_2$-MP, (D) Pd/P25-BM, (E) PdCl$_2$/TiO$_2$-BM, (F) Pd(NO$_3$)$_2$/TiO$_2$-BM and (G) Pure TiO$_2$ P90. (b) Effect of the Pd loading on H$_2$ production rate for Pd/TiO$_2$-BM at a contact time of 0.14 s (c) Hydrogen photoproduction rates of Pd/TiO$_2$-BM under different milling time (orange bars), milling frequency (yellow bars) and ball to powder ratio (BPR, grey bars); all samples were prepared by changing only one parameter in each experiment while keeping the other ball milling conditions unchanged. (d) Recyclability tests of Pd/TiO$_2$-BM, Pd/TiO$_2$-IWI and Pure P90. Error bars correspond to standard deviation of three measurements.

tin oxide (FTO) glass loaded with Pd/TiO$_2$-BM, Pd/TiO$_2$-IWI, Pd/TiO$_2$-BMC or Pure P90 was used as the working electrode. The coating procedure was performed as follows: firstly, the FTO glass was washed three times alternately with absolute ethanol and acetone. Then, 15 mg of each sample was dispersed in 1.5 mL of absolute ethanol under ultra-sounds for 30 min, and the slurry was then deposited onto the FTO glass with a spin-coater and dried at room temperature. An Ag/AgCl (3.5 M) electrode (+0.205 V vs. NHE at 25 °C) and a Pt wire (~3.6 cm^2) were used as reference electrode and counter electrode, respectively. The system was stabilized under open circuit potential (OCP) for 1 h before each test. Electrochemical impedance spectroscopy (EIS) analysis was conducted at 10 mV amplitude relative to OCP (0.3 V vs. NHE) with the frequency ranging from 1 MHz to 10 mHz. A UV lamp emitting at 365 ± 5 nm was chosen as the light source and the resistance values were ac-quired both under UV irradiation and dark conditions for each sample. Transient photocurrent responses were performed at a bias potential of 10 mV (vs. OCP) under on-off cyclic UV light exposure at 20 s intervals by manual chopping. Mott-Schottky measurements (M-S) were recorded in the range of −0.8–0.5 V at an amplitude of 10 mV and a fixed fre-quency of 1 kHz with the presence and absence of UV illumination. According to the M-S equation (Eq. (1)), the flat band potential (V_{fb}) value can be determined by extrapolating the plot to the x-axis to ach-ieve the horizontal intercept (C^{-2} =0).

$$C^{-2} = \frac{2}{N_D \varepsilon \varepsilon_0 e} \left(V - V_{fb} - \frac{kT}{e} \right) \tag{1}$$

where C is the space-charge capacitance, N_D represents the charge

carrier density, ε and ε_0 are the relative permittivity and vacuum permittivity of the semiconductor, respectively, e is the elementary charge, V is the applied potential, V_{fb} is the flat band potential, k is the Boltzmann constant, and T is the absolute temperature. As the e= 1.6 × 10^{-19} C, ε_0= 8.85 × 10^{-12} F m^{-1}, ε= 55 for TiO$_2$ [38], k = 1.38 × 10^{-23} m^2 kg s^{-2} K^{-1}, the charge carrier densities of all measured photocatalysts can be calculated via Eq. (1). The conduction band position (E$_{CB}$) was estimated through Eq. (2).

$$E_{CB} - E_F = kTln\left(\frac{N_C}{N_D}\right) \tag{2}$$

where the E_F is the Fermi level position (E_F=V_{fb}) and N_C is the effective density of states in the conduction band calculated by Eq. (3) to get the value of 7.7 × 10^{20} cm^{-3}.

$$N_C = 2\left(\frac{2\pi m_{de}kT}{h^2}\right)^{\frac{3}{2}} \tag{3}$$

h is Planck constant and m_{de} is the density-of-state effective mass for electrons of TiO$_2$ (9.1 × 10^{-30} kg).

2.6. Photocatalytic H$_2$ evolution experiments

The photocatalytic performance was measured in a tubular glass photoreactor (40 mL) equipped with a UV light source containing four LEDs emitting at 365 ± 5 nm (from SACOPA, S.A.U.) at atmospheric pressure and room temperature under dynamic conditions (Fig. S1), as
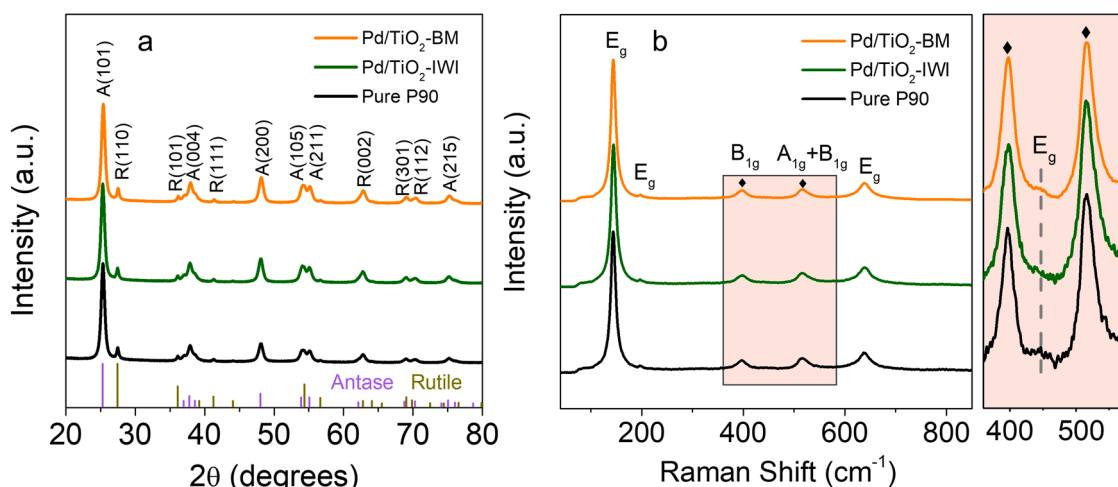
Fig. 2. XRD patterns (a) and Raman spectra (b) of Pd/TiO$_2$-BM, Pd/TiO$_2$-IWI and Pure P90.

elsewhere reported [39]. 87.5 g water and 9.92 g ethanol were mixed in a saturator (Dreschel bottle) and bubbled by an argon gas stream (20 mL min^{-1}) to form a gaseous mixture of water:ethanol:Ar (water: ethanol=9:1 molar), which was introduced into the photoreactor (continuous flow). The gas hourly space velocity (GHSV) was ca. 26, 000 h^{-1} (contact time of 0.14 s). 2.0 mg (unless otherwise stated) of each prepared photocatalyst were dispersed in absolute ethanol and sonicated for 10 min. The homogeneous suspension was drop-casted onto a circular cellulose paper (2.54 cm^2) and dried at 50 °C for 1 h. Then, the impregnated paper was placed between the two parts of the glass photoreactor accompanied with an O-ring. The photoreactor was sealed with parafilm and a circular clamp. The UV light source was aligned to a synthetic quartz glass cylindrical lens towards the exposed photocatalyst in the setup. An UV irradiation of 82 ± 0.5 mW cm^{-2} was measured on the sample by a UVA radiation monitor (Solar Light Co.). Gaseous products were monitored on-line every 4 min with a micro-gas chromatograph (GC, Agilent 490) employing three columns: Stabilwax, MS 5 Å and Plot U. Calibration curves were obtained in the concentration range of each product using standard gas mixtures provided by certified mass flow controllers (Bronkhorst) and following standard procedures. Only the production of hydrogen and acetaldehyde in equimolar amounts was observed in our experiments, indicating that the only process taking place was the photodehydrogenation reaction of ethanol. No CO$_2$ was produced, indicating the absence of photo-reforming [40]. The apparent quantum yield (AQY) was estimated based on the Eq. (4):

$$AQY \quad (\%) = \frac{2N_{H_2}}{N_P} \quad \times 100 \tag{4}$$

where N_{H2} represents the number of hydrogen molecules generated and N_P is the number of incident photons reaching the photocatalyst [39,41].

## 3. Results and discussion

3.1. Photocatalytic activity

For a rational comparison of photocatalyst performances and AQY determination, in addition to a fixed contact time, the effect of the amount of photocatalyst should be taken into consideration because the photocatalytic performance is heavily affected by both mass and photon transfer limitations. For this reason, an initial series of experiments with different Pd/TiO$_2$-BM loading weight were conducted to confirm the optimum photon usage. As shown in Fig. S2, the H$_2$ evolution rate achieved an optimal value at the photocatalyst amount of 2.0 mg, and after that, the H$_2$ production rate did not improve with the increase of

sample loading. Therefore, a weight of 2.0 mg of photocatalyst was chosen throughout this study. To evaluate the photocatalytic behaviour of Pd-decorated TiO$_2$ photocatalysts, a series of comparative experiments were performed over the samples prepared by ball milling with different TiO$_2$ and Pd precursors (TiO$_2$ P90, P25, PdCl$_2$ and Pd(NO$_3$)$_2$) (Fig. 1a). As a support material, TiO$_2$ P90 presented a better photo-catalytic performance than TiO$_2$ P25, owing to its higher surface area, which is beneficial to increase the dispersion of the Pd co-catalyst spe-cies and, therefore, improve the contact with gaseous reactants and active sites during the photoreaction process. The photocatalyst pre-pared from palladium acetate showed a better photocatalytic perfor-mance with respect to those samples prepared from Pd(NO$_3$)$_2$ or PdCl$_2$. Thus, palladium acetate was chosen as the Pd precursor at the following stage of our research and 1.0 wt% of Pd loading showed the best result (Fig. 1b). Analysis by ICP-OES revealed that all samples contained a similar Pd loading of 0.9 ± 0.1 wt%, which was similar to the theoret-ical value of 1.0 wt%.

We also investigated the effect of the different milling parameters on H$_2$ production. It is well-known that the ball-milling procedure greatly influences the textural properties of the supported catalyst material (such as the surface area [42,43] and/or defects [44,45]) and the existing forms of the cocatalyst metals (such as their oxidation state and dispersion). Firstly, we confirmed by XPS analyses (Fig. S3) that the employed stainless-steel jar and balls did not introduce any contami-nation in the ball-milled samples. The crucial effects of milling param-eters on the photocatalytic activity were confirmed by a number of experimental observations (see Fig. 1c). The results show that a milling time of 10 min yields the highest value of H$_2$ production. The effect of the milling frequency was also studied by keeping constant the milling time and BPR values at 10 min and 45, respectively. As illustrated in Fig. 1c, the photocatalytic performance was strongly dependent on the milling frequency: the higher the frequency the lower the rate of H$_2$ production. This suggests that low impact velocities favour an effective metal-support interaction. It is worth noting that the photocatalyst prepared by manual grinding (Pd/TiO$_2$-MP) exhibited a remarkable rate of H$_2$ production of 77.7 mmol h^{-1} g^{-1}, which can be ascribed to the mechanical energy introduced by soft grinding via mortar and pestle. The BPR value is another important parameter that deserves attention [46]. As shown in Fig. 1c, a BPR value of 45 was found as the optimum ratio to achieve the highest H$_2$ production rate under the experimental conditions tested (the milling process is also influenced by the filling ratio of the vial where the mechanochemical process takes place [47, 48]).

The ball milled photocatalyst Pd/TiO$_2$-BM produced under the optimal conditions was tested in four consecutive hydrogen
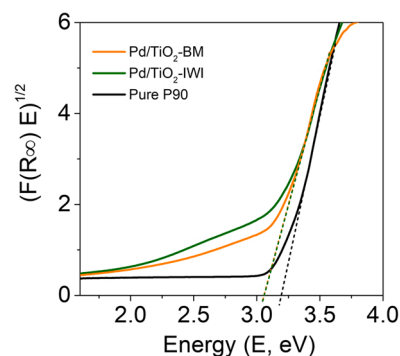
Fig. 3. Tauc plots of $(F(R_\infty)E)^{1/2}$ versus E(eV) for Pd/TiO$_2$-BM, Pd/TiO$_2$-IWI and Pure P90, including a linear fit (dashed lines) to determine the band gap energy (E$_g$).

photoproduction stages of 60 min, keeping a pause window of 30 min without UV light irradiation before starting the next reaction stage. The obtained hydrogen production profile was compared with the sample obtained by conventional incipient wetness impregnation method (Pd/TiO$_2$-IWI) and pristine TiO$_2$ P90 as references, as shown in Fig. 1d. The BM sample exhibited a considerable initial hydrogen evolution rate, about 1.6 times higher than that of the IWI sample (86.7 mmol h^{-1} g^{-1} versus 55.6 mmol h^{-1} g^{-1}). Insignificant H$_2$ production rates (3.1 mmol h^{-1} g^{-1}) were obtained over pure P90, confirming the action of Pd species as effective cocatalysts. Whereas we observed an initial deactivation from the first to the second photoreaction stage, both BM

and IWI samples stabilized their hydrogen production rates in subsequent photoreaction stages, demonstrating the reusability of the photocatalyst, which is of interest for practical applications. It is worth to mention that compared to our previous Au clusters/TiO$_2$ system [36], the Pd/TiO$_2$-BM not only shows a significant improvement of the photocatalytic hydrogen production rate, from 49.3 to 86.7 mmol h^{-1} g^{-1}, but also an excellent enhancement in the stability: whereas a 74% of the initial hydrogen production rate remained stable after the third reaction stage employing Au clusters/TiO$_2$ [36], this value increased to 85% when Pd/TiO$_2$-BM was used as a photocatalyst. With the aim of further investigating the long-term stability of the different Pd/TiO$_2$ photocatalysts, independent 48 h and 100 h photocatalytic tests were carried out, as shown in Fig. S4a and S4b, respectively. During all the experiments, the sample Pd/TiO$_2$-BM showed a clear superior photoactivity compared to Pd/TiO$_2$-IWI, even if the sample prepared by ball milling showed a stronger initial deactivation during the first hours. It is concluded that the Pd/TiO$_2$-BM owns the merit for long-term durability.

3.2. Characterization of photocatalysts

The crystalline phases of Pd/TiO$_2$-BM, Pd/TiO$_2$-IWI and TiO$_2$ (P90) were analysed by X-ray diffraction (XRD) as presented in Fig. 2a. All the XRD patterns exhibit the typical diffraction peaks of TiO$_2$. The reflections at 2θ values of 25.3°, 37.9°, 48.1°, 54.2°, 55.1° and 75.2° are attributed to the (101), (004), (200), (105), (211) and (215) crystal planes of anatase (JCPDS No. 21-1272), respectively. The peaks at 2θ values of 27.5°, 36.1°, 41.4°, 62.8°, 69.0° and 70.3° correspond to the (110), (101), (111), (002), (301) and (112) crystal planes of rutile phase
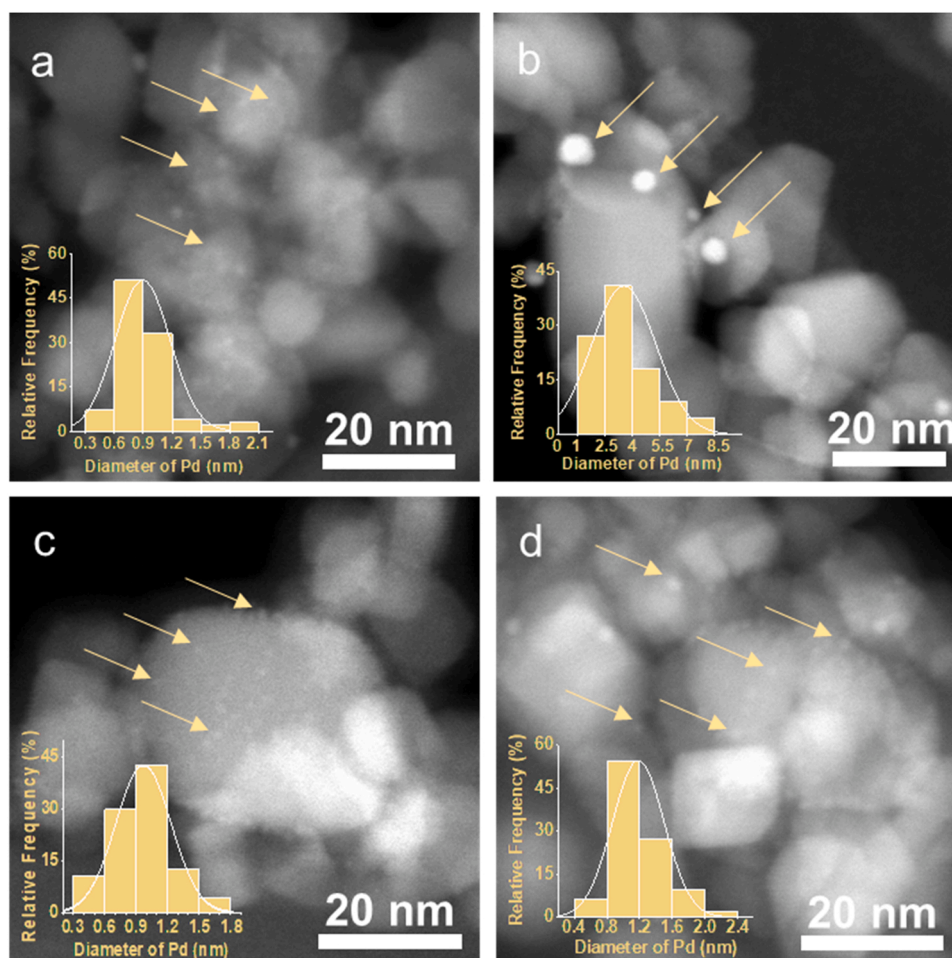
Fig. 4. HAADF-STEM images of Pd/TiO$_2$-BM: (a) fresh and (b) after reaction; Pd/TiO$_2$-IWI: (c) fresh and (d) after reaction.
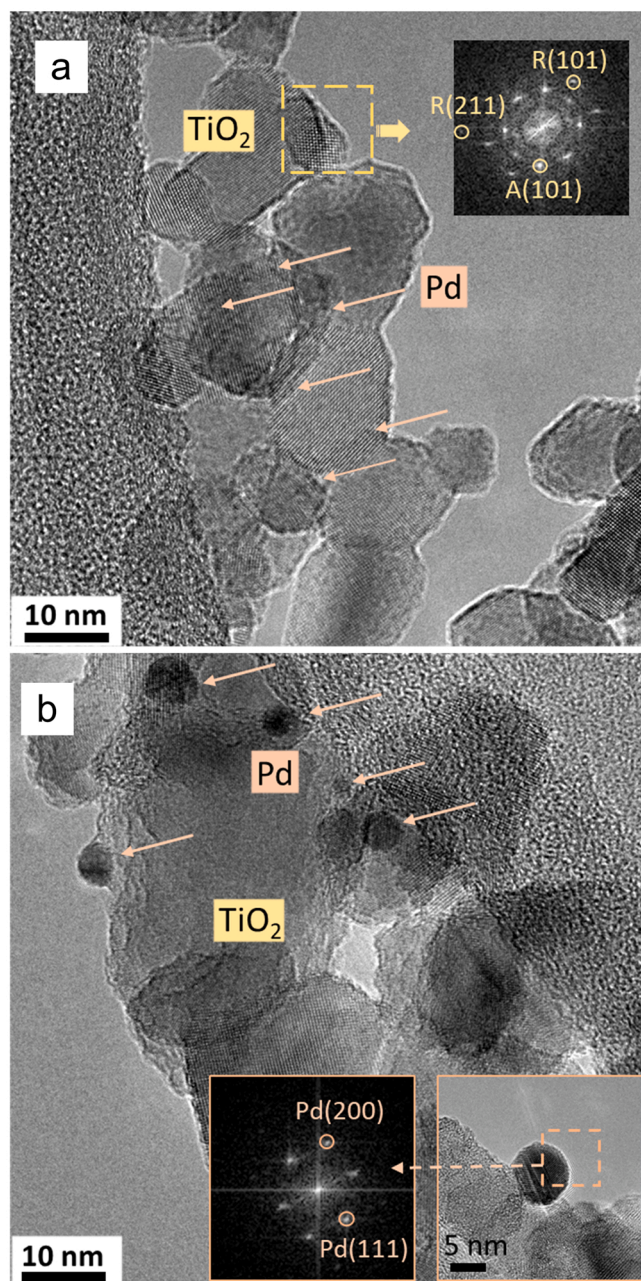
Fig. 5. HRTEM images of Pd/TiO$_2$-BM fresh (a) and after reaction (b). The insets in (a) and (b) show Fourier Transform (FT) images corresponding to the crystal planes of anatase, rutile and palladium, respectively.

(JCPDS No. 21-1276). No Pd-related features were observed in the XRD patterns due to the low content of the metal. The mean crystallite sizes of TiO$_2$ in pure P90, Pd/TiO$_2$-BM and Pd/TiO$_2$-IWI estimated from the FWHM of the anatase (101) line by the Scherrer equation are around 13–14 nm, in accordance with the SEM results (Fig. S5). These results demonstrate that the mechanochemical preparation method used in this study does not affect the crystal structure of TiO$_2$. Fig. 2b shows the Raman spectra recorded for the as-prepared photocatalysts. Five phonon vibrational peaks located at 143.8 cm^{-1} (E$_g$), 196.3 cm^{-1} (E$_g$), 396.6 cm^{-1} (B$_{1g}$), 516.5 cm^{-1} (A$_{1g}$ + B$_{1g}$) and 638.1 cm^{-1} (E$_g$) are observed in all samples, which correspond well to the anatase phase [49]. A small shoulder can be observed at 446.8 cm^{-1} (E$_g$) (see the enlarged plot area in Fig. 2b), which is associated to the rutile phase [50]. For the main E$_g$ peak of anatase, there is no significant shift or broadenings in either milled or impregnated samples, which means that

no significant defects in the titania structure are induced by the ball milling process.

Tauc plots were used to calculate the band gap energy (E$_g$) of each sample, as shown in Fig. 3 (the UV spectra employed to obtain the Tauc plots are shown in Fig. S6). The E$_g$ values are 3.20, 3.08 and 3.07 eV for P90, Pd/TiO$_2$-BM and Pd/TiO$_2$-IWI, respectively. It is interesting to note that the incorporation of Pd resulted in a significant decrease of the band gap energy in comparison with the bare TiO$_2$. This phenomenon is ascribed to the characteristic absorption of surface excitation caused by the plasmon effect of metals [51,52], which leads to an enhanced light absorption towards the visible region (Fig. S6).

A detailed HAADF-STEM (Fig. 4) and HRTEM (Fig. 5) study was conducted to compare the Pd/TiO$_2$-BM and Pd/TiO$_2$-IWI samples as prepared and after photoreaction tests. The dispersion and mean size of Pd for both fresh BM and IWI samples were similar (Fig. 4a and c), ranging from about 0.6–1.2 nm. EDX spectra confirmed the presence of Pd (Fig. S7). It is noteworthy that after photoreaction, the Pd clusters of the Pd/TiO$_2$-BM sample were more prone to agglomerate and Pd clusters evolved into nanoparticles of about 2.5–4 nm (Fig. 4b). The HRTEM images of Pd/TiO$_2$-BM fresh and after reaction (Fig. 5) provide a direct evidence for this transformation. Fig. 5a shows Pd clusters (indicated by arrows) highly dispersed on the surface of TiO$_2$. After one hour of photoreaction under UV light (365 nm), the Pd clusters grew and originated Pd nanoparticles (Fig. 5b). The FT inset in Fig. 5b shows spots corresponding to a Pd metal nanoparticle oriented along the [110] crystallographic direction. This is accompanied by a slightly decrease in the rate of hydrogen evolution (see Fig. 1d). In contrast, the Pd clusters in the sample Pd/TiO$_2$-IWI did not significantly grow after photoreaction (Fig. 5d). However, even if the Pd clusters agglomerate in the sample Pd/TiO$_2$-BM under photoreaction conditions, it showed a much better photocatalytic performance than Pd/TiO$_2$-IWI (Figs. 1d and S4). This is a clear indication that the ball milling method originates a particular and unprecedented architecture between the TiO$_2$ support and Pd, which is responsible for an enhanced photocatalytic activity. It is worth noting that the HAADF-STEM and HRTEM images also confirmed the existence of ultrasmall Pd clusters (mostly less than 1 nm) well dispersed on the surface of samples PdCl$_2$/TiO$_2$-BM and Pd(NO$_3$)$_2$/TiO$_2$-BM, as shown in Fig S8. However, the rate of hydrogen evolution did not reach the same level as that of Pd/TiO$_2$-BM, probably due to the presence of surface chloride/nitrate residues after the milling procedure and/or to a different metal-support interaction.

X-ray photoelectron spectroscopy (XPS) was used to probe the interaction between Pd species and the TiO$_2$ support in further detail. The collected Pd 3d, Ti 2p, and O 1s spectra are presented in Fig. 6. As a reference, we also conducted the XPS analysis on the sample Pd/TiO$_2$-BMC, which was synthesized by ball milling followed by a calcination step at 300 °C for 3 h under air atmosphere (the same treatment as that for the IWI sample). The deconvoluted Pd 3d signal (Fig. 6a) clearly illustrates the different oxidation states of Pd existing on the surface of the different photocatalysts. In the sample Pd/TiO$_2$-BM, Pd 3d$_{5/2}$ peaks with binding energies at around 335.0 eV, 336.0 eV and 337.2 eV can be ascribed to metallic Pd (Pd^0), Pd^{2+} and Pd^{4+} species, respectively [53], where the metallic Pd was the dominant species (51.1%). In contrast, in samples Pd/TiO$_2$-IWI and Pd/TiO$_2$-BMC, palladium was mostly in oxidized form. Due to the similitude between the XP spectra of Pd/TiO$_2$-IWI and Pd/TiO$_2$-BMC, the photocatalytic H$_2$ production of the sample Pd/TiO$_2$-BMC was also measured (Figs. S4 and S9), and the photocatalytic behaviour was indistinguishable from that of Pd/TiO$_2$-IWI. Furthermore, the HAADF-STEM images (Fig. S10) revealed that the changes of Pd particle size in sample Pd/TiO$_2$-BMC occurred during photoreaction are in line with those of Pd/TiO$_2$-IWI. The similarity between samples Pd/TiO$_2$-IWI and Pd/TiO$_2$-BMC indicated that the particular architecture of the Pd-TiO$_2$ interphase, which is responsible of the photocatalytic performance, was lost after a thermal treatment at moderate temperature. On the other hand, the higher amount of reduced Pd species recorded by XPS in Pd/TiO$_2$-BM before
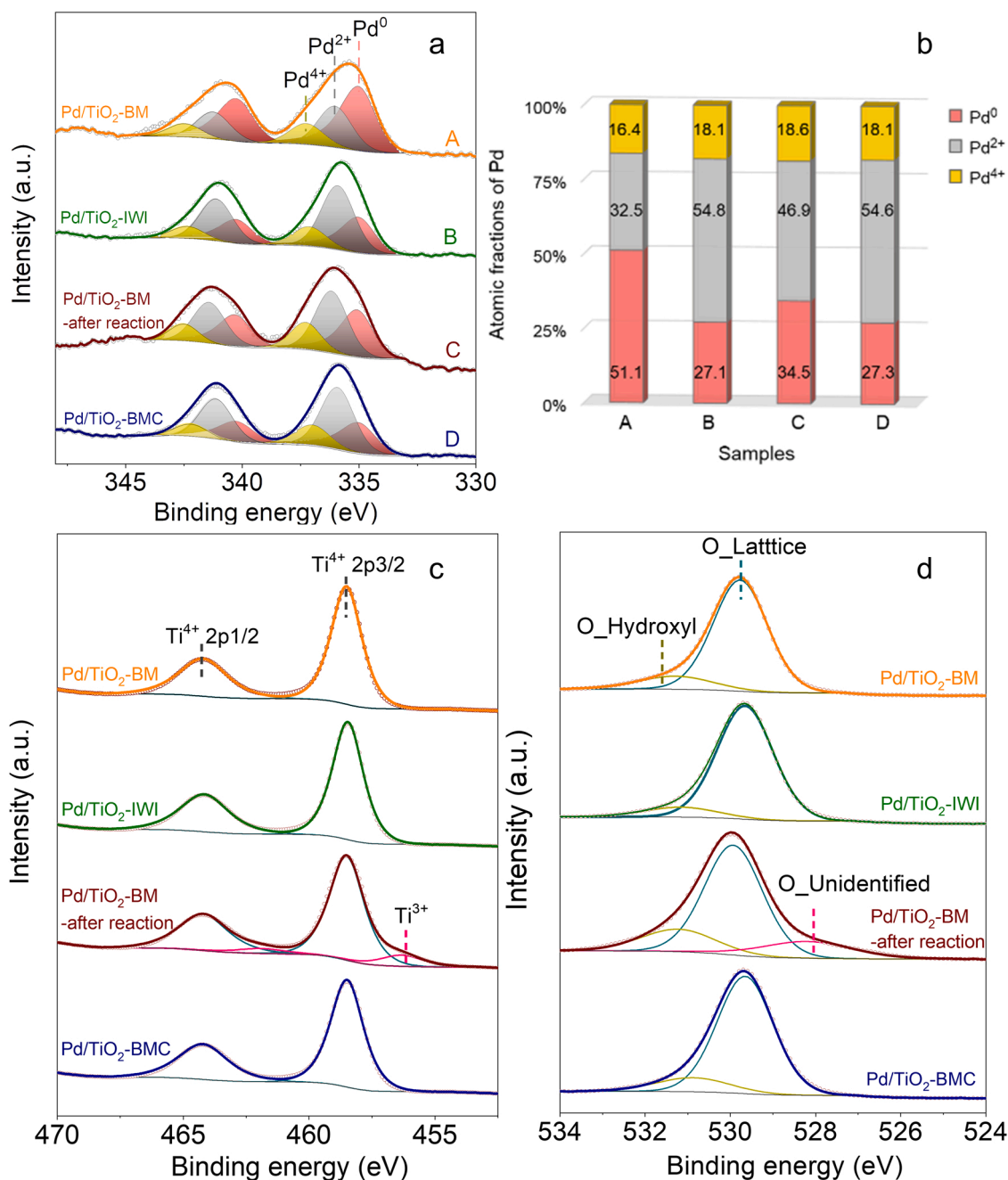
Fig. 6. XP Pd 3d (a), Ti 2p (c) and O 1s (d) spectra of Pd/TiO$_2$-BM, Pd/TiO$_2$-IWI, Pd/TiO$_2$-BM-after reaction and Pd/TiO$_2$-BMC. (b): the corresponding atomic ratios of the different Pd oxidation states extracted from the XP spectra in (a).

and after reaction (Fig. 6b), suggested that the hydrogen evolution is favoured by metallic Pd, which is more effective for electron transfer between Pd and TiO$_2$ [54]. For the sake of clarity, we recorded the Raman spectra (Fig. S11a) and XRD pattern (Fig. S12) of Pd/TiO$_2$-BMC, which were identical to those of Pd/TiO$_2$-BM and Pd/TiO$_2$-IWI samples, indicating similar characteristics for the TiO$_2$ support. We believe that during the ball milling process, the local high temperature resulting from the impact and friction between the ball, vessel and powders, easily decomposed palladium acetate into metallic Pd clusters, which were immediately anchored on the TiO$_2$ support (sample Pd/TiO$_2$-BM). Under UV illumination, these ultrasmall Pd clusters aggregated into Pd nanoparticles due to their large surface area and high surface energy. Meanwhile, this transformation also triggered the partial oxidation of the palladium particles, and further kept a particular interaction with

the support, which was responsible for the sustained superior photocatalytic performance. Therefore, the mechanochemical method provides a novel and simple route to prepare TiO$_2$-based samples with enhanced photocatalytic properties. Additionally, the Ti 2p and O 1s XP spectra were also analysed. Fig. 6c depicts two different peaks centred at 458.5 and 464.2 eV in all samples, corresponding to the 2p$_{3/2}$ and 2p$_{1/2}$ of Ti^{4+} state of TiO$_2$. In addition, in sample Pd/TiO$_2$-BM-after reaction, there are two additional signals at lower binding energy at 456.4 and 461.6 eV, which can be identified as 2p$_{3/2}$ and 2p$_{1/2}$ of Ti^{3+} state [55]. These are accompanied by an additional peak at 528.2 eV in the O 1s spectrum, which is correlated with the presence of Ti^{3+} [56,57]. The peaks located at 529.7 eV and 531.2 eV in the O 1s spectra of all samples are assigned to lattice oxygen and surface hydroxyl groups (O-H), respectively [58]. Interestingly, the loss of oxygen of TiO$_2$ surface and
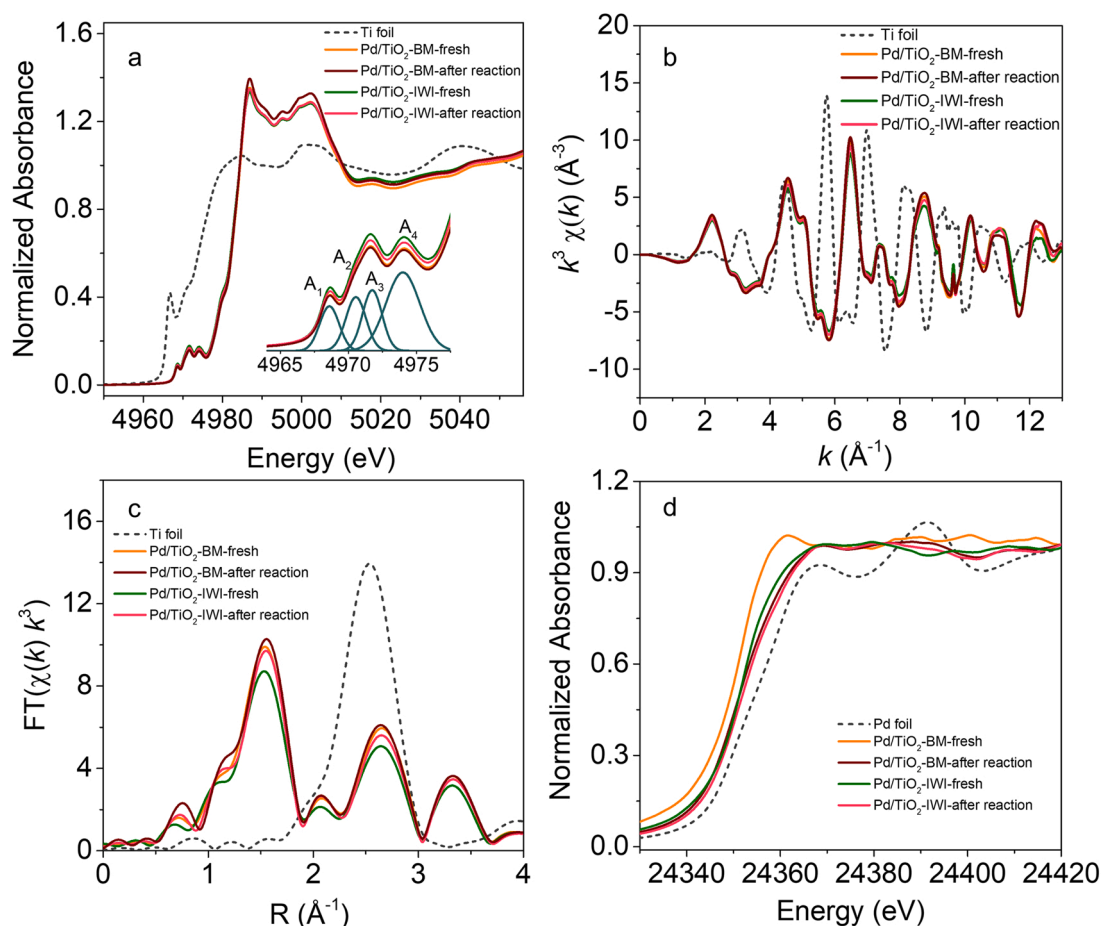
Fig. 7. Normalized X-ray absorption near edge structure (XANES, a: Ti K-edge; d: Pd K-edge), k space (b) and Fourier transforms of k^3-weighted Ti K-edge (c) of Ti foil, Pd/TiO$_2$-BM (fresh and after reaction) and Pd/TiO$_2$-IWI (fresh and after reaction) (no phase correction). The inset of Fig. a shows the magnified pre-edge peak and the corresponding contribution from the regions A$_1$, A$_2$, A$_3$ and A$_4$ obtained after a Gaussian fitting.

the increase of the oxidation state of Pd occurred simultaneously in Pd/TiO$_2$-BM after the photoreaction under UV irradiation. We speculate that oxygen atoms of TiO$_2$ were captured by Pd NPs at the metal-oxide interface under the photoreaction environment, resulting in a distinct and strong metal-support interaction.

To study the bulk structure of TiO$_2$, we performed Ti K-edge X-ray absorption near-edge structure (XANES) and extended X-ray absorption fine structure (EXAFS) experiments, as shown in Fig. 7. The normalized XANES spectra show that all the Pd/TiO$_2$-BM and Pd/TiO$_2$-IWI samples exhibit a similar characteristic line shape in both the pre-edge region (4964–4980 eV) and white line peaks. The pre-edge peaks were confirmed to be four peaks by fitting with Gaussian functions, labelled as A$_1$, A$_2$, A$_3$, and A$_4$, as shown the inset of Fig. 7a [59–61]. These four dominant features are referred to the structure of Ti cations in octahedral sites in anatase TiO$_2$ (Ti^{4+}) [62]. The peaks A$_1$, A$_2$, A$_3$, and A$_4$ are attributed to a quadrupole transition of 1s–3d (t$_{2g}$), a dipole transition from 1s to hybridized 3d (t$_{2g}$)–4p, a quadrupole transition from 1s to hybridized 3d (e$_g$), and a dipole transition from 1s to hybridized 3d (e$_g$)–4p, respectively [60,63]. There are no distinct structural features among all the samples studied, both in their fresh state and after reaction, implying that both the ball milling and impregnation preparation methods did not affect the bulk of TiO$_2$ based-materials. The Ti K-edge EXAFS data in k space and Fourier-transformed (FT) k^3-weighted data are shown in Fig. 7b and c without phase correction, providing a more detailed quantitative analysis of coordination environments of Ti. The fitted curves and corresponding parameters are shown in Fig. S13 and Table S1. The EXAFS oscillations in k space appeared identical for all samples. The FTs revealed that the Ti first neighbour shell is dominated

by Ti-O scattering at approximately 1.6 Å (non-phase correction) with an average coordination number (CNs) of $(5.3–5.6) \pm 0.5$ (see Table S1), which corresponds well to the theoretical number of Ti-O bonds in pure TiO$_2$ (CN=6). In addition, the second Ti-Ti shells were located at around 2.65 Å, with CNs in line with the theoretical value of 4 of pure TiO$_2$. Therefore, EXAFS data shows that the original local structural geometry of TiO$_6$ octahedron in TiO$_2$ is preserved in all cases. It also suggests that no defects or oxygen vacancies were introduced into the bulk material of TiO$_2$ during the milling process, in agreement with XRD and Raman. These results, together with the fact that Ti(III) and O-Ti(III) species are encountered by XPS, suggests that the existence of Ti(III) in the sample Pd/TiO$_2$-BM after reaction is restricted at the surface of the photocatalyst as a result of a particular interaction between Pd and the support.

The normalized Pd K-edge XANES spectra are shown in Fig. 7d. Exceptionally, the absorption of the fresh Pd/TiO$_2$-BM sample is significantly shifted to low energy values. In general, the absorption edge energy of oxidized Pd is higher than that of metallic Pd [64–66]. In the present case, however, this unusual negative shift is ascribed to the formation of a particular interaction between small Pd clusters and the titania support, also in accordance to the XPS results.

To provide the intrinsic photoelectrochemical properties of TiO$_2$ P90, Pd/TiO$_2$-BM, Pd/TiO$_2$-IWI and Pd/TiO$_2$-BMC, the electrochemical impedance spectra (EIS, Nyquist plots) were acquired under UV irradiation ($\lambda = 365$ nm, Fig. 8a) and dark condition (Fig. S14a). The electron transfer resistance was strongly reduced after the introduction of Pd NPs onto the TiO$_2$ surface and was quite sensitive to the preparation method. The radius of the semicircle of Pd/TiO$_2$-BM is significantly smaller than
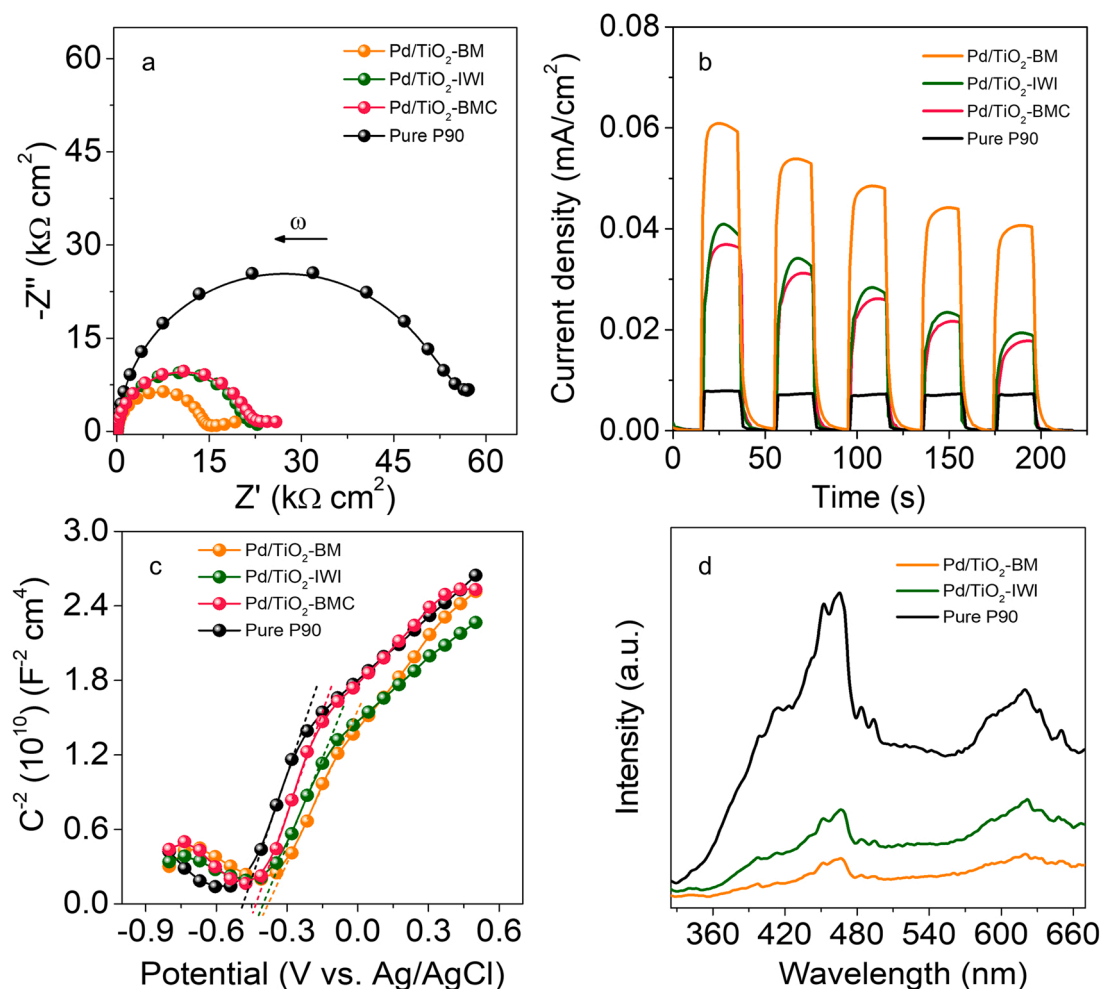
Fig. 8. Nyquist plots under UV irradiation, $\lambda = 365$ nm (a), transient photocurrent response, $\lambda = 365$ nm (b), Mott-Schottky plots under dark condition (c), and photoluminescence spectra, $\lambda_{ex}= 300$ nm (d).

those of the other photocatalysts, implying a low electron transfer resistance and, thus, a superior charge separation efficiency. The transient photocurrent responses shown in Fig. 8b confirmed that the presence of Pd promoted the migration of carriers with respect to the pristine TiO_2 P90. They also showed that the photocatalysts followed exactly the same trend as in the EIS analysis. These results demonstrated that the particular interaction between the Pd clusters and TiO_2 in the Pd/TiO_2-BM sample facilitated the photocurrent generation, which in turn explained the higher hydrogen photogeneration rate observed for Pd/TiO_2-BM. Interestingly, the calcination of Pd/TiO_2-BM yielded a

photocatalytic material that exhibited exactly the same resistance as the conventional Pd/TiO_2-IWI sample and, accordingly, both samples yielded exactly the same hydrogen photogeneration rate (Fig. 1d). Again, these results pointed out to the existence of a unique Pd-TiO_2 architecture formed by mechanochemistry in Pd/TiO_2-BM, which was lost after calcination.

Considering that the work functions of most of noble metals are higher than the work functions of n-type semiconductors (including TiO_2), a Schottky junction can be built up through the intimate contact of a semiconductor with a metal, consequently promoting charge

Table 1
Electron carrier density (N_D), flat band potential (V_{fb}), conduction band (E_{CB}) and valence band (E_{VB}) calculated for TiO_2 P90, Pd/TiO_2-BM, Pd/TiO_2-IWI and Pd/TiO_2-BMC.

	TiO_2 P90		Pd/TiO_2-BM		Pd/TiO_2-IWI		Pd/TiO_2-BMC	
	UV	Dark	UV	Dark	UV	Dark	UV	Dark
N_D (*10^{19} cm^{-3})[a]	4.7	4.6	5.7	6.9	5.7	6.1	4.3	4.8
V_{fb} (V vs. NHE)[b]	-0.29	-0.29	-0.21	-0.18	-0.27	-0.20	-0.21	-0.23
E_{CB}-E_F (V vs. NHE)[c]	0.072	0.072	0.067	0.062	0.067	0.065	0.074	0.071
E_{CB} (V vs. NHE)	-0.36	-0.36	-0.27	-0.24	-0.33	-0.26	-0.28	-0.30
Eg (eV)	3.20		3.08		3.07		3.06	
E_{VB} (V vs. NHE)[d]	2.84	2.84	2.81	2.84	2.74	2.81	2.78	2.76

[a] calculated from Eq. (1).
[b] measured from M-S plots in Fig. 8c.
[c] calculated from Eq. (2).
[d] calculated by $E_{VB}=E_g+E_{CB}$

separation [67,68]. In our study, the Pd entities were anchored directly on the surface of TiO_2, so that the electron transfer could occur at the interface between the conduction band of TiO_2 and Pd, establishing a new equilibrium state between their Fermi levels. Then the electrons accumulated on the Pd surface would be consumed via the photoreduction reaction. To identify the donor density (N_D) and flat band potential (V_{fb}) of the different photocatalysts, Mott-Schottky (M-S) measurements were carried out, which are shown in Fig. 8c (dark condition) and Fig. S14b (under UV light). The carrier density can be estimated from the slope of the M-S plots in Fig. 8c by Eq. (1), obtaining similar values for all samples within the range of $(5.6 \pm 1.3) \times 10^{19}$ cm^{-3}. The V_{fb} values are determined by the intercept of the linear parts of M-S plots on the potential axis. Table 1 compiles the values of electron carrier density (N_D), flat band potential (V_{fb}), conduction band (E_{CB}) and valence band (E_{VB}) calculated for pure TiO_2, Pd/TiO_2-BM, Pd/TiO_2-IWI and Pd/TiO_2-BMC samples. The sample Pd/TiO_2-BM presents a more pronounced positive shift of V_{fb} with respect to pristine TiO_2 than other photocatalysts, implying a more decrease in bending of band edge, thus boosting the electron- injection and -transfer efficiency [69–72]. Additionally, we explored the efficiency of charge separation, transfer and trapping over TiO_2, Pd/TiO_2-BM and Pd/TiO_2-IWI through an analysis of the photoluminescence (PL) spectra, as shown in Fig. 8d. It is deduced that the decoration of Pd on the TiO_2 surface provokes a dramatic quenching of PL intensity at around 465 nm with respect to that of bare TiO_2 P90, suggesting that the presence of anchored Pd species effectively suppresses the undesirable recombination of electron-hole pairs in TiO_2 and, consequently, promotes the photoreaction. The lowest PL intensity of Pd/TiO_2-BM indicates the lowest recombination rate and the longest lifetime of photogenerated carriers, in close agreement with the results of the electrochemical measurements and in accordance with the highest photoproduction rate of hydrogen.

To sum up, the comprehensive characterization of the different Pd/TiO_2 samples elucidated the enhanced photocatalytic activity of the mechanochemically anchored Pd clusters onto TiO_2 nanoparticles, which exhibited a particular and unprecedented metal-support interaction. Moreover, we also demonstrated a dynamic rearrangement phenomenon of small Pd clusters evolving into Pd nanoparticles under the photocatalytic conditions tested, which has been decisive for determining the actual nature of active Pd species. Therefore, mechanochemical synthesis not only represents an extremely easy, cheap, fast and solvent-free method for preparing materials for photocatalytic applications, but it also allows to access unprecedented and highly active sites characterized by a particular metal-support interaction for the hydrogen evolution reaction. In our case, this is particularly evident from the XPS, XANES and EXAFS results, which show a particular synergy between Pd and TiO_2. Particularly appealing is the observation by HAADF-STEM and HRTEM that, even if the Pd clusters agglomerate in the sample prepared by ball milling under photoreaction conditions, the photocatalytic performance is much better than that of TiO_2 decorated with Pd nanoparticles by conventional methods (including long-term stability tests). Clearly, the ball milling method gives rise to a particular and unprecedented architecture between the TiO_2 support and Pd, which promotes the migration of carriers (photocurrent generation) with respect to the pristine TiO_2 and is responsible for an improved photocatalytic activity.

4. Conclusions

In this work, Pd clusters supported on TiO_2 were fabricated by a facile, green and one-step ball milling procedure at room temperature. The ultrasmall Pd species were well dispersed on the surface of TiO_2 as observed from HRTEM and HAADF-STEM images. This Pd/TiO_2-BM photocatalyst displayed a great improvement on photocatalytic H_2 production rates in comparison with the sample prepared by the conventional wet chemical method (around 1.6 times higher). The dominant Pd species generated from milling process were in metallic states

(51.1%), as shown in the Pd 3d XP spectra, which resulted in an impressive contribution on the separation of photogenerated electron-hole pairs. Interestingly, a special interaction effect was created between Pd clusters and titania support in Pd/TiO_2-BM photocatalysts during the photocatalytic process under UV illumination, which can be properly interpreted from the changes in the surface detected in XP Ti 2p and O 1s spectra and the bulk analysis of the Pd K-edge XANES spectra. Importantly, this particular metal-oxide interface played a crucial role in Pd stabilization for the further photocatalytic reaction, resulting in an outstanding activity over longer testing times. The mechanochemical strategy may open up new perspectives for manufacturing stable metal clusters supported over oxides as enhanced catalysts without employing any organic ligand to stabilize the active sites. Therefore, mechanochemical methods appear as feasible candidates to substitute conventional synthesis procedures that involve the usage of chemical stabilizers in the synthesis of catalytic supported clusters.

CRediT authorship contribution statement

Yufen Chen: Investigation, Methodology, Formal analysis, Data curation, Writing – original draft preparation. **Lluís Soler**: Conceptualization, Supervision, Investigation, Methodology, Data curation, Writing – review & editing. **Marina Armengol-Profitós:** Formal analysis, Data curation, Writing – review & editing. **Chenyang Xie**: Formal analysis, Writing – review & editing. **Daniel Crespo:** Formal analysis, Writing – review & editing. **Jordi Llorca:** Conceptualization, Supervision, Investigation, Methodology, Data curation, Writing – review & editing.

Declaration of Competing Interest

The authors declare that they have no known competing financial interests or personal relationships that could have appeared to influence the work reported in this paper.

Acknowledgments

Appendix A. Supporting information

Supplementary data associated with this article can be found in the online version at doi:10.1016/j.apcatb.2022.121275.

References

[1] T. Wang, X. Tao, X. Li, K. Zhang, S. Liu, B. Li, Synergistic Pd single atoms, clusters, and oxygen vacancies on TiO_2 for photocatalytic hydrogen evolution coupled with selective organic oxidation, Small 17 (2021) 1–10, https://doi.org/10.1002/smll.202006255.

[2] B. Sarkar, P. Prajapati, R. Tiwari, R. Tiwari, S. Ghosh, S. Shubhra Acharyya, C. Pendem, R. Kumar Singha, L.N. Sivakumar Konathala, J. Kumar, T. Sasaki, R. Bal, Room temperature selective oxidation of cyclohexane over Cu-nanoclusters supported on nanocrystalline Cr_2O_3, Green Chem. 14 (2012) 2600–2606, https://doi.org/10.1039/c2gc35658a.

[3] E. Kowalska, H. Remita, C. Colbeau-Justin, J. Hupka, J. Belloni, Modification of titanium dioxide with platinum ions and clusters: application in photocatalysis, J. Phys. Chem. C 112 (2008) 1124–1131, https://doi.org/10.1021/jp077466p.

[4] F.X. Xiao, Z. Zeng, S.H. Hsu, S.F. Hung, H.M. Chen, B. Liu, Light-induced in situ transformation of metal clusters to metal nanocrystals for photocatalysis, ACS

Appl. Mater. Interfaces 7 (2015) 28105–28109, https://doi.org/10.1021/acsami.5b09091.

[5] L. Liu, A. Corma, Confining isolated atoms and clusters in crystalline porous materials for catalysis, Nat. Rev. Mater. 6 (2021) 244–263, https://doi.org/10.1038/s41578-020-00250-3.

[6] Z. Luo, A.W. Castleman, S.N. Khanna, Reactivity of metal clusters, Chem. Rev. 116 (2016) 14456–14492, https://doi.org/10.1021/acs.chemrev.6b00230.

[7] T. Imaoka, Y. Akanuma, N. Haruta, S. Tsuchiya, K. Ishihara, T. Okayasu, W. J. Chun, M. Takahashi, K. Yamamoto, Platinum clusters with precise numbers of atoms for preparative-scale catalysis, Nat. Commun. 8 (2017) 1–8, https://doi.org/10.1038/s41467-017-00800-4.

[8] A. Corma, P. Concepción, M. Boronat, M.J. Sabater, J. Navas, M.J. Yacaman, E. Larios, A. Posadas, M.A. López-Quintela, D. Buceta, E. Mendoza, G. Guilera, A. Mayoral, Exceptional oxidation activity with size-controlled supported gold clusters of low atomicity, Nat. Chem. 5 (2013) 775–781, https://doi.org/10.1038/nchem.1721.

[9] E. Bus, R. Prins, J.A. van Bokhoven, Origin of the cluster-size effect in the hydrogenation of cinnamaldehyde over supported Au catalysts, Catal. Commun. 8 (2007) 1397–1402, https://doi.org/10.1016/j.catcom.2006.11.040.

[10] W.E. Kaden, T. Wu, W.A. Kunkel, S.L. Anderson, Electronic structure controls reactivity of size-selected Pd clusters adsorbed on TiO_2 surfaces, Science 326 (2009) 826–829, https://doi.org/10.1126/science.1180297.

[11] B.C. Gates, Supported metal clusters: synthesis, structure, and catalysis, Chem. Rev. 95 (1995) 511–522, https://doi.org/10.1021/cr00035a003.

[12] M.J. Kale, P. Christopher, Utilizing quantitative in situ FTIR spectroscopy to identify well-coordinated Pt atoms as the active site for CO oxidation on Al_2O_3-supported Pt catalysts, ACS Catal. 6 (2016) 5599–5609, https://doi.org/10.1021/acscatal.6b01128.

[13] J. Liu, Catalysis by supported single metal atoms, ACS Catal. 7 (2017) 34–59, https://doi.org/10.1021/acscatal.6b01534.

[14] J. Liu, B.R. Bunes, L. Zang, C. Wang, Supported single-atom catalysts: synthesis, characterization, properties, and applications, Environ. Chem. Lett. 16 (2018) 477–505, https://doi.org/10.1007/s10311-017-0679-2.

[15] B. Weng, K.Q. Lu, Z. Tang, H.M. Chen, Y.J. Xu, Stabilizing ultrasmall Au clusters for enhanced photoredox catalysis, Nat. Commun. 9 (2018) 1543–1553, https://doi.org/10.1038/s41467-018-04020-2.

[16] R. Jin, Y. Cao, C.A. Mirkin, K.L. Kelly, G.C. Schatz, J.G. Zheng, Photoinduced conversion of silver nanospheres to nanoprisms, Science 294 (2001) 1901–1903, https://doi.org/10.1126/science.1066541.

[17] L. Piccolo, Restructuring effects of the chemical environment in metal nanocatalysis and single-atom catalysis, Catal. Today 373 (2021) 80–97, https://doi.org/10.1016/j.cattod.2020.03.052.

[18] A. Gołąbiewska, A. Malankowska, M. Jarek, W. Lisowski, G. Nowaczyk, S. Jurga, A. Zaleska-Medynska, The effect of gold shape and size on the properties and visible light-induced photoactivity of Au-TiO_2, Appl. Catal. B Environ. 196 (2016) 27–40, https://doi.org/10.1016/j.apcatb.2016.05.013.

[19] T.W. Hansen, A.T. Delariva, S.R. Challa, A.K. Datye, Sintering of catalytic nanoparticles: particle migration or ostwald ripening? Acc. Chem. Res. 46 (2013) 1720–1730, https://doi.org/10.1021/ar3002427.

[20] G.P. Lee, Y. Shi, E. Lavoie, T. Daeneke, P. Reineck, U.B. Cappel, D.M. Huang, U. Bach, Light-driven transformation processes of anisotropic silver nanoparticles, ACS Nano 7 (2013) 5911–5921, https://doi.org/10.1021/nn4013059.

[21] B. Weng, Y. Jiang, H.G. Liao, M.B.J. Roeffaers, F. Lai, H. Huang, Z. Tang, Visualizing light-induced dynamic structural transformations of Au clusters-based photocatalyst via in situ TEM, Nano Res. 14 (2021) 2805–2809, https://doi.org/10.1007/s12274-021-3289-z.

[22] S. Liu, Y.J. Xu, Photo-induced transformation process at gold clusters-semiconductor interface: implications for the complexity of gold clusters-based photocatalysis, Sci. Rep. 6 (2016) 1–13, https://doi.org/10.1038/srep22742.

[23] I. Piwoński, K. Spilarewicz-Stanek, A. Kisielewska, K. Kadzioła, M. Cichomski, J. Ginter, Examination of Ostwald ripening in the photocatalytic growth of silver nanoparticles on titanium dioxide coatings, Appl. Surf. Sci. 373 (2016) 38–44, https://doi.org/10.1016/j.apsusc.2016.01.131.

[24] M. El-Roz, I. Telegeiev, N.E. Mordvinova, O.I. Lebedev, N. Barrier, A. Behilil, M. Zaarour, L. Lakiss, V. Valtchev, Uniform generation of sub-nanometer silver clusters in zeolite cages exhibiting high photocatalytic activity under visible light, ACS Appl. Mater. Interfaces 10 (2018) 28702–28708, https://doi.org/10.1021/acsami.8b09634.

[25] Y.S. Chen, P.V. Kamat, Glutathione-capped gold nanoclusters as photosensitizers. visible light-induced hydrogen generation in neutral water, J. Am. Chem. Soc. 136 (2014) 6075–6082, https://doi.org/10.1021/ja5017365.

[26] R. Murugan, R. Peri, P. Pandurangan, M. Bhagavathiachari, Light-harvesting property from self-assembly of cobalt nanocluster aggregates for efficient hydrogen evolution, J. Phys. Chem. C 124 (2020) 2258–2264, https://doi.org/10.1021/acs.jpcc.9b08546.

[27] P.D. Jadzinsky, G. Calero, C.J. Ackerson, D.A. Bushnell, R.D. Kornberg, Structure of a thiol monolayer-protected gold nanoparticle at 1.1 Å resolution, Science 318 (2007) 430–433, https://doi.org/10.1126/science.1148624.

[28] A. Ledo-Suárez, J. Rivas, C.F. Rodríguez-Abreu, M.J. Rodríguez, E. Pastor, A. Hernández-Creus, S.B. Oseroff, M.A. López-Quintela, Facile synthesis of stable subnanosized silver clusters in microemulsions, Angew. Chem. Int. Ed. 46 (2007) 8823–8827, https://doi.org/10.1002/anie.200702427.

[29] S. Wu, H. Zeng, Z.A. Schelly, Growth of uncapped, subnanometer size gold clusters prepared via electroporation of vesicles, J. Phys. Chem. B 109 (2005) 18715–18718, https://doi.org/10.1021/jp0543476.

[30] R. Ye, A.V. Zhukhovitskiy, C.V. Deraedt, F.D. Toste, G.A. Somorjai, Supported dendrimer-encapsulated metal clusters: toward heterogenizing homogeneous catalysts, Acc. Chem. Res. 50 (2017) 1894–1901, https://doi.org/10.1021/acs.accounts.7b00232.

[31] H. Tsunoyama, H. Sakurai, Y. Negishi, T. Tsukuda, Size-specific catalytic activity of polymer-stabilized gold nanoclusters for aerobic alcohol oxidation in water, J. Am. Chem. Soc. 127 (2005) 9374–9375, https://doi.org/10.1021/ja052161e.

[32] Z. Zhang, S. Yang, X. Hu, H. Xu, H. Peng, M. Liu, B.P. Thapaliya, K. Jie, J. Zhao, J. Liu, H. Chen, Y. Leng, X. Lu, J. Fu, P. Zhang, S. Dai, Mechanochemical nonhydrolytic sol-gel-strategy for the production of mesoporous multimetallic oxides, Chem. Mater. 31 (2019) 5529–5536, https://doi.org/10.1021/acs.chemmater.9b01244.

[33] M.J. Rak, T. Friščić, A. Moores, One-step, solvent-free mechanosynthesis of silver nanoparticle-infused lignin composites for use as highly active multidrug resistant antibacterial filters, RSC Adv. 6 (2016) 58365–58370, https://doi.org/10.1039/c6ra03711a.

[34] M.F. Thorne, M.L.R. Gómez, A.M. Bumstead, S. Li, T.D. Bennett, Mechanochemical synthesis of mixed metal, mixed linker, glass-forming metal-organic frameworks, Green Chem. 22 (2020) 2505–2512, https://doi.org/10.1039/d0gc00546k.

[35] A.D. Katsenis, A. Puškarić, V. Štrukil, C. Mottillo, P.A. Julien, K. Užarević, M. H. Pham, T.O. Do, S.A.J. Kimber, P. Lazić, O. Magdysyuk, R.E. Dinnebier, I. Halasz, T. Friščić, In situ X-ray diffraction monitoring of a mechanochemical reaction reveals a unique topology metal-organic framework, Nat. Commun. 6 (2015) 6662, https://doi.org/10.1038/ncomms7662.

[36] Y. Chen, L. Soler, C. Xie, X. Vendrell, J. Serafin, D. Crespo, J. Llorca, A straightforward method to prepare supported Au clusters by mechanochemistry and its application in photocatalysis, Appl. Mater. Today 21 (2020), 100873, https://doi.org/10.1016/j.apmt.2020.100873.

[37] M. Danielis, L.E. Betancourt, I. Orozco, N.J. Divins, J. Llorca, J.A. Rodríguez, S. D. Senanayake, S. Colussi, A. Trovarelli, Methane oxidation activity and nanoscale characterization of Pd/CeO_2 catalysts prepared by dry milling Pd acetate and ceria, Appl. Catal. B Environ. 282 (2021), 119567, https://doi.org/10.1016/j.apcatb.2020.119567.

[38] E. Thimsen, A.B.F. Martinson, J.W. Elam, M.J. Pellin, Energy levels, electronic properties, and rectification in ultrathin p-NiO films synthesized by atomic layer deposition, J. Phys. Chem. C 116 (2012) 16830–16840, https://doi.org/10.1021/jp302008k.

[39] A. May-Masnou, L. Soler, M. Torras, P. Salles, J. Llorca, A. Roig, Fast and simple microwave synthesis of TiO_2/Au nanoparticles for gas-phase photocatalytic hydrogen generation, Front. Chem. 6 (2018) 110–122, https://doi.org/10.3389/fchem.2018.00110.

[40] A.K. Wahab, M.A. Nadeem, H. Idriss, Hydrogen production during ethylene glycol photoreactions over Ag-Pd/TiO_2 at different partial pressures of oxygen, Front. Chem. 7 (2019) 1–16, https://doi.org/10.3389/fchem.2019.00780.

[41] C. Xing, Y. Liu, Y. Zhang, X. Wang, P. Guardia, L. Yao, X. Han, T. Zhang, J. Arbiol, L. Soler, Y. Chen, K. Sivula, N. Guijarro, A. Cabot, J. Llorca, A direct Z-scheme for the photocatalytic hydrogen production from a water ethanol mixture on $CoTiO_3$/TiO_2 heterostructures, ACS Appl. Mater. Interfaces 13 (2021) 449–457, https://doi.org/10.1021/acsami.0c17004.

[42] A.E.D. Mahmoud, A. Stolle, M. Stelter, Sustainable synthesis of high-surface-area graphite oxide via dry ball milling, ACS Sustain. Chem. Eng. 6 (2018) 6358–6369, https://doi.org/10.1021/acssuschemeng.8b00147.

[43] P. Dzik, T. Svoboda, J. Kaštyl, M. Veselý, Modification of photocatalyst morphology by ball milling and its impact on the physicochemical properties of wet coated layers, Catal. Today 328 (2019) 65–70, https://doi.org/10.1016/j.cattod.2019.01.051.

[44] X. Zhou, N. Liu, J. Schmidt, A. Kahnt, A. Osvet, S. Romeis, E.M. Zolnhofer, V.R. R. Marthala, D.M. Guldi, W. Peukert, M. Hartmann, K. Meyer, P. Schmuki, Noble-metal-free photocatalytic hydrogen evolution activity: the impact of ball milling anatase nanopowders with TiH_2, Adv. Mater. 29 (2017), 1604747, https://doi.org/10.1002/adma.201604747.

[45] R. Eckert, M. Felderhoff, F. Schüth, Preferential carbon monoxide oxidation over copper-based catalysts under in situ ball milling, Angew. Chem. Int. Ed. 56 (2017) 2445–2448, https://doi.org/10.1002/anie.201610501.

[46] M. Wang, Q. Zhao, H. Yang, D. Shi, J. Qian, Photocatalytic antibacterial properties of copper doped TiO_2 prepared by high-energy ball milling, Ceram. Int. 46 (2020) 16716–16724, https://doi.org/10.1016/j.ceramint.2020.03.246.

[47] N.R. Mojarrad, R. Kheirifard, R.T. Mousavian, Y. Afkham, S. Nakisa, Filling ratio of vial: an important parameter for ball milling, J. Therm. Anal. Calorim. 126 (2016) 1097–1103, https://doi.org/10.1007/s10973-016-5635-z.

[48] P. Kuziora, M. Wyszyńska, M. Polanski, J. Bystrzycki, Why the ball to powder ratio (BPR) is insufficient for describing the mechanical ball milling process, Int. J. Hydrog. Energy 39 (2014) 9883–9887, https://doi.org/10.1016/j.ijhydene.2014.03.009.

[49] T.S. Dörr, L. Deilmann, G. Haselmann, A. Cherevan, P. Zhang, P. Blaha, P.W. de Oliveira, T. Kraus, D. Eder, Ordered mesoporous TiO_2 gyroids: effects of pore architecture and Nb-doping on photocatalytic hydrogen evolution under UV and visible irradiation, Adv. Energy Mater. 8 (2018) 1–11, https://doi.org/10.1002/aenm.201802566.

[50] M.G. Rinaudo, A.M. Beltrán, M.A. Fernández, L.E. Cadús, M.R. Morales, Tailoring materials by high-energy ball milling: TiO_2 mixtures for catalyst support application, Mater. Today Chem. 17 (2020), 100340, https://doi.org/10.1016/j.mtchem.2020.100340.

[51] S. Yurani, T. Camacho, A. Rey, M.D. Hernández-alonso, J. Llorca, F. Medina, S. Contreras, Pd/TiO_2-WO_3 photocatalysts for hydrogen generation from water-

methanol mixtures, Appl. Surf. Sci. 455 (2018) 570–580, https://doi.org/10.1016/j.apsusc.2018.05.122.

[52] L. Martínez, M. Benito, I. Mata, L. Soler, E. Molins, J. Llorca, Preparation and photocatalytic activity of Au/TiO₂ lyogels for hydrogen production, Sustain, Energy Fuels 2 (2018) 2284–2295, https://doi.org/10.1039/c8se00293b.

[53] B. Jin, X. Ye, H. Zhong, F. Jin, Light-driven hydrogenation of bicarbonate into formate over nano-Pd/TiO₂, ACS Sustain. Chem. Eng. 8 (2020) 6798–6805, https://doi.org/10.1021/acssuschemeng.0c01616.

[54] D.S. Selishchev, N.S. Kolobov, A.V. Bukhtiyarov, E.Y. Gerasimov, A.I. Gubanov, D. V. Kozlov, Deposition of Pd nanoparticles on TiO₂ using a Pd(acac)₂ precursor for photocatalytic oxidation of CO under UV-LED irradiation, Appl. Catal. B Environ. 235 (2018) 214–224, https://doi.org/10.1016/j.apcatb.2018.04.074.

[55] A.C. Bronneberg, C. Höhn, R. Van De Krol, Probing the interfacial chemistry of ultrathin ALD-grown TiO₂ films: an in-line XPS study, J. Phys. Chem. C 121 (2017) 5531–5538, https://doi.org/10.1021/acs.jpcc.6b09468.

[56] Z. Pap, É. Karácsonyi, Z. Cegléd, A. Dombi, V. Danciu, I.C. Popescu, L. Baia, A. Oszkó, K. Mogyorósi, Dynamic changes on the surface during the calcination of rapid heat treated TiO₂ photocatalysts, Appl. Catal. B Environ. 111–112 (2012) 595–604, https://doi.org/10.1016/j.apcatb.2011.11.012.

[57] H. Idriss, On the wrong assignment of the XPS O1s signal at 531–532 eV attributed to oxygen vacancies in photo- and electro-catalysts for water splitting and other materials applications, Surf. Sci. 712 (2021) 2–7, https://doi.org/10.1016/j.susc.2021.121894.

[58] L. Liu, X. Gu, Y. Cao, X. Yao, L. Zhang, C. Tang, F. Gao, L. Dong, Crystal-plane effects on the catalytic properties of Au/TiO₂, ACS Catal. 3 (2013) 2768–2775, https://doi.org/10.1021/cs400492w.

[59] K.S. Yang, Y.R. Lu, Y.Y. Hsu, C.J. Lin, C.M. Tseng, S.Y.H. Liou, K. Kumar, D.H. Wei, C.L. Dong, C.L. Chen, Plasmon-induced visible-light photocatalytic activity of Au nanoparticle-decorated hollow mesoporous TiO₂: a view by X-ray spectroscopy, J. Phys. Chem. C 122 (2018) 6955–6962, https://doi.org/10.1021/acs.jpcc.8b00205.

[60] J.W. Wu, C.H. Chen, C.J. Lin, K. Kumar, Y.R. Lu, S. Ya Hsuan Liou, S.Y. Chen, D. H. Wei, C. Li Dong, C.L. Chen, Improved photocatalytic efficacy of TiO₂ open nanotube arrays: a view by XAS, Appl. Surf. Sci. 527 (2020) 2–7, https://doi.org/10.1016/j.apsusc.2020.146844.

[61] P.C. Angelomé, L. Andrini, M.E. Calvo, F.G. Requejo, S.A. Bilmes, G.J.A.A. Soler-Illia, Mesoporous anatase TiO₂ films: Use of Ti K XANES for the quantification of the nanocrystalline character and substrate effects in the photocatalysis behavior, J. Phys. Chem. C 111 (2007) 10886–10893, https://doi.org/10.1021/jp069020z.

[62] P. Renōnes, L. Collado, A. Iglesias-Juez, F.E. Oropeza, F. Fresno, V.A. De La Penā O'Shea, Silver-gold bimetal-loaded TiO₂ photocatalysts for CO₂ reduction, Ind. Eng. Chem. Res. 59 (2020) 9440–9450, https://doi.org/10.1021/acs.iecr.0c01034.

[63] H.W. Kuo, C.J. Lin, H.Y. Do, R.Y. Wu, C.M. Tseng, K. Kumar, C.L. Dong, C.L. Chen, Electronic and atomic structure of TiO₂ anatase spines on sea-urchin-like microspheres by X-ray absorption spectroscopy, Appl. Surf. Sci. 502 (2020), 144297, https://doi.org/10.1016/j.apsusc.2019.144297.

[64] P. Liu, Y. Zhao, R. Qin, L. Gu, P. Zhang, G. Fu, N. Zheng, A vicinal effect for promoting catalysis of Pd₁/TiO₂: supports of atomically dispersed catalysts play more roles than simply serving as ligands, Sci. Bull. 63 (2018) 675–682, https://doi.org/10.1016/j.scib.2018.03.002.

[65] H. Xiong, M.H. Wiebenga, C. Carrillo, J.R. Gaudet, H.N. Pham, D. Kunwar, S.H. Oh, G. Qi, C.H. Kim, A.K. Datye, Design considerations for low-temperature hydrocarbon oxidation reactions on Pd based catalysts, Appl. Catal. B Environ. 236 (2018) 436–444, https://doi.org/10.1016/j.apcatb.2018.05.049.

[66] C. Wang, C. Wen, J. Lauterbach, E. Sasmaz, Superior oxygen transfer ability of Pd/MnOx-CeO₂ for enhanced low temperature CO oxidation activity, Appl. Catal. B Environ. 206 (2017) 1–8, https://doi.org/10.1016/j.apcatb.2017.01.020.

[67] S. Bai, J. Jiang, Q. Zhang, Y. Xiong, Steering charge kinetics in photocatalysis: Intersection of materials syntheses, characterization techniques and theoretical simulations, Chem. Soc. Rev. 44 (2015) 2893–2939, https://doi.org/10.1039/c5cs00064e.

[68] X. Yang, S. Zhang, H. Tao, X. Yan, Y. Tan, Y. Zhang, S. Gao, R. Cao, Visible-light-driven selective alcohol dehydrogenation and hydrogenolysis: via the Mott Schottky effect, J. Mater. Chem. A 8 (2020) 6854–6862, https://doi.org/10.1039/c9ta13811k.

[69] Y. Wang, Y.Y. Zhang, J. Tang, H. Wu, M. Xu, Z. Peng, X.G. Gong, G. Zheng, Simultaneous etching and doping of TiO₂ nanowire arrays for enhanced photoelectrochemical performance, ACS Nano 7 (2013) 9375–9383, https://doi.org/10.1021/nn4040876.

[70] M. Ye, J. Gong, Y. Lai, C. Lin, Z. Lin, High-efficiency photoelectrocatalytic hydrogen generation enabled by palladium quantum dots-sensitized TiO₂ nanotube arrays, J. Am. Chem. Soc. 134 (2012) 15720–15723, https://doi.org/10.1021/ja307449z.

[71] X. Lü, X. Mou, J. Wu, D. Zhang, L. Zhang, F. Huang, F. Xu, S. Huang, Improved-performance dye-sensitized solar cells using Nb-doped TiO₂ electrodes: efficient electron Injection and transfer, Adv. Funct. Mater. 20 (2010) 509–515, https://doi.org/10.1002/adfm.200901292.

[72] Z. Zhang, Y. Yu, P. Wang, Hierarchical top-porous/bottom-tubular TiO₂ nanostructures decorated with Pd nanoparticles for efficient photoelectrocatalytic decomposition of synergistic pollutants, ACS Appl. Mater. Interfaces 4 (2012) 990–996, https://doi.org/10.1021/am201630s.